# Selective Photodissociation of Acetonitrile Ligands in Ruthenium Polypyridyl Complexes Studied by Density Functional Theory

Yi-Jung Tu,[†] Shivnath Mazumder,[†] John F. Endicott,[†] Claudia Turro,[‡] Jeremy J. Kodanko,[†] and H. Bernhard Schlegel*,[†]

[†]Department of Chemistry, Wayne State University, 5101 Cass Avenue, Detroit, Michigan 48202, United States
[‡]Department of Chemistry and Biochemistry, The Ohio State University, Columbus, Ohio 43210, United States

Ⓢ Supporting Information

ABSTRACT: Metal complexes that release ligands upon photoexcitation are important tools for biological research and show great potential as highly specific therapeutics. Upon excitation with visible light, $[Ru(TQA)(MeCN)_2]^{2+}$ [TQA = tris(2-quinolinylmethyl)amine] exchanges one of the two acetonitriles (MeCNs), whereas $[Ru(DPAbpy)MeCN]^{2+}$ [DPAbpy = N-(2,2′-bipyridin-6-yl)-N,N-bis(pyridin-2-ylmethyl)amine] does not release MeCN. Furthermore, $[Ru(TQA)(MeCN)_2]^{2+}$ is highly selective for release of the MeCN that is perpendicular to the plane of the two axial quinolines. Density functional theory calculations provide a clear explanation for the photodissociation behavior of these two complexes. Excitation by visible light and intersystem crossing leads to a six-coordinate ^{3}MLCT state. Dissociation of acetonitrile can occur after internal conversion to a dissociative ^{3}MC state, which has an occupied $d\sigma^*$ orbital that interacts in an antibonding fashion with acetonitrile. For $[Ru(TQA)(MeCN)_2]^{2+}$, the dissociative ^{3}MC state is lower than the ^{3}MLCT state. In contrast, the ^{3}MC state of $[Ru(DPAbpy)MeCN]^{2+}$ that releases acetonitrile has an energy higher than that of the ^{3}MLCT state, indicating dissociation is unfavorable. These results are consistent with the experimental observations that efficient photodissociation of acetonitrile occurs for $[Ru(TQA)(MeCN)_2]^{2+}$ but not for $[Ru(DPAbpy)MeCN]^{2+}$. For the release of the MeCN ligand in $[Ru(TQA)(MeCN)_2]^{2+}$ that is perpendicular to the axial quinoline rings, the ^{3}MLCT state has an occupied quinoline π^* orbital that can interact with a $d\sigma^*$ Ru−NCCH$_3$ antibonding orbital as the Ru−NCCH$_3$ bond is stretched and the quinolines bend toward the departing acetonitrile. This reduces the barrier for the formation of the dissociative ^{3}MC state, leading to the selective photodissociation of this acetonitrile. By contrast, when the acetonitrile is in the plane of the quinolines or bpy, no interaction occurs between the ligand π^* orbital and the $d\sigma^*$ Ru−NCCH$_3$ orbital, resulting in high barriers for conversion to the corresponding ^{3}MC structures and no release of acetonitrile.
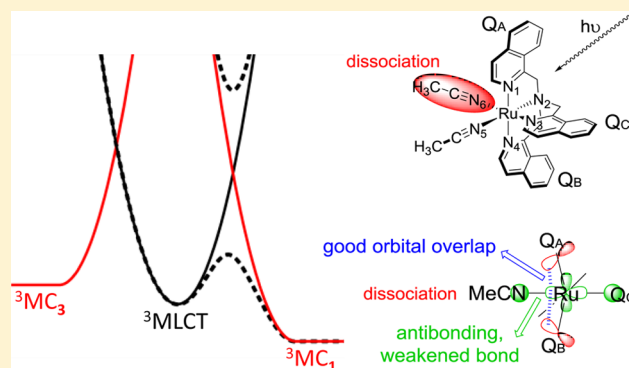
INTRODUCTION

Metal complexes that undergo photochemical substitution reactions are used widely in chemistry and biology.[1−4] Photodissociation can release active agents from metal centers, providing a method for garnering spatiotemporal control over biological activity.[5−7] Light-activated release of ligands can also open up coordination sites for interaction with biological targets.[8,9] In general, light-activated metal complexes are important tools for basic research applications.[10] They also have potential as highly specific agents for photodynamic therapy that would mitigate damage to surrounding tissue by using light with a targeted photosensitizer to control the site of drug activation.[11−13]

Light-activated ruthenium complexes have been applied successfully in many biological applications, in part because of their kinetic inertness in the dark and rich photochemical reactivity. Photoactivation can be used to open coordination sites on ruthenium for DNA binding, such as that observed for

$[Ru(bpy)_2(NH_3)_2]^{2+}$ (bpy = 2,2′-bipyridine)[14] and other complexes.[15] Recent reports showed that bidentate ligands can also be released from Ru(II) complexes for DNA binding, providing high phototoxicity indices against cancer cells under light versus dark conditions.[16,17] Ruthenium complexes also photocleave DNA through oxidative mechanisms.[18−21] Beyond DNA,[22] a variety of small molecules can be caged and released from ruthenium complexes, including nitric oxide (NO),[23−30] neurotransmitters,[31−41] cytotoxic agents,[5,6] and protease inhibitors.[42,43] These complexes have proven applications in cell culture experiments for garnering spatial and temporal control over biological activities, such as apoptotic induction, neurotransmission, or enzyme inhibition.

Although ruthenium complexes have enjoyed great success as biochemical tools, ligands for ruthenium-based caging groups

have focused mainly on planar heteroaromatics of lower denticity, typically bi- or tridentate chelators such as bpy or tpy (tpy = 2,2′:6′,2″-terpyridine). In an effort to explore additional chemical space, Kodanko, Turro, and co-workers recently discovered that tris(2-pyridylmethyl)amine (TPA), a tripodal chelator with four nitrogen donors, is an effective ligand for ruthenium-based caging groups. Complexes derived from TPA are stable in the dark and release nitriles efficiently upon irradiation with UV light (365 nm).[44] In an effort to tune the photochemistry of the Ru(TPA) caging group, ligands derived from TPA were designed and analyzed for photochemical reactivity of Ru(II) nitrile complexes.[45] Results revealed that absorptivity is shifted readily into the visible range upon tuning the ligand structure. However, a wide range of reactivities with light was observed for complexes derived from very similar ligands, even though several complexes absorbed light in the visible range. Further investigations were needed to explain why some complexes underwent selective ligand release, whereas others were inert toward light.

In general, two factors are important for achieving efficient release of a ligand from a metal complex useful for biological applications. First, the complex should absorb at the desired wavelength of light. Second, after excitation into a ^{1}MLCT band, the excited state should undergo conversion into an excited state where ligand dissociation occurs. For Ru(II) complexes, it is generally accepted that excitation into a singlet MLCT (^{1}MLCT) state results in intersystem crossing into a triplet MLCT (^{3}MLCT) state, which then undergoes a transition to a triplet metal-centered (^{3}MC) potential energy surface where ligand dissociation occurs.[46−48] The mechanism of dissociation of the ligand from [Ru(bpy)$_2$L$_2$]$^{2+}$ complexes has been studied by density functional theory (DFT),[47] and ligand dissociation was attributed to the mixing between ^{3}MLCT and ^{3}MC dissociative states.[46−48] However, the factors that controlled the photochemical reactivity of Ru complexes derived from TPA and related ligands were not clear and warrant further investigation.

In this paper, we apply DFT to investigate the photochemical behavior of two Ru complexes from Kodanko, Turro, and co-workers that were identified by photodissociation experiments: Ru(TQA) {[Ru(TQA)(MeCN)$_2$]$^{2+}$, where TQA = tris(2-quinolinylmethyl)amine} and Ru(DPAbpy) {[Ru(DPAbpy)-MeCN]$^{2+}$, where DPAbpy = N-(2,2′-bipyridin-6-yl)-N,N-bis-(pyridin-2-ylmethyl)amine}. The relative energies of the ^{3}MLCT and ^{3}MC structures were studied first. Then relaxed scans were conducted on the triplet potential energy surfaces to determine the barriers for dissociation. The molecular orbitals of the ^{3}MLCT and ^{3}MC structures were examined to explain the contrasting photodissociation behaviors of the Ru(TQA) and Ru(DPAbpy) complexes.

■ COMPUTATIONAL METHODS

Electronic structure calculations were conducted using the BP86 density functional[50,51] as implemented in a developmental version of Gaussian.[52] The SDD basis set and effective core potential[53−55] were used for the Ru atom, and the 6-31G(d) basis set[56,57] was used for all other atoms. All optimized structures were checked by normal mode vibrational analysis, and wave functions were tested for SCF stability. Solvation effects in acetonitrile and water were accounted for using the implicit SMD continuum solvation model[58] and were included during structure optimization. The identities of the ^{3}MLCT and ^{3}MC electronic configurations were confirmed by spin density populations. GaussView[59] was used to visualize isodensity plots of the spin populations (isovalue = 0.004 au) and canonical and corresponding/

biorthogonal orbitals[60] (isovalue = 0.04 au). To explore the potential energy surfaces for dissociation, relaxed potential energy surface scans were performed by stretching the Ru−NCCH$_3$ bond and optimizing the remaining coordinates. The QST3 method[61,62] was used to find the transition state on the triplet surface. The transition state was confirmed to have only one imaginary frequency by vibrational mode analysis. The DVV steepest descent reaction path following was used to track the dissociation on the ^{3}MC surface.[63] TD-DFT calculations[64,65] were performed with the same density functional and basis sets. Vertical excitations with 25 singlet and 25 triplet states were calculated using ground state geometries to simulate the UV−vis spectra. To explore the triplet potential energy surfaces, 20 triplet excited states were calculated using the geometries from the relaxed scan. The electronic transitions were checked by visualizing the orbitals (isovalue = 0.04 au) using GaussView.

■ RESULTS AND DISCUSSION

The [Ru(TQA)(MeCN)$_2$]$^{2+}$ and [Ru(DPAbpy)(MeCN)]$^{2+}$ complexes shown in Scheme 1 were previously synthesized

Scheme 1. Ru(TQA) and Ru(DPAbpy) Complexes with Atom Numbering
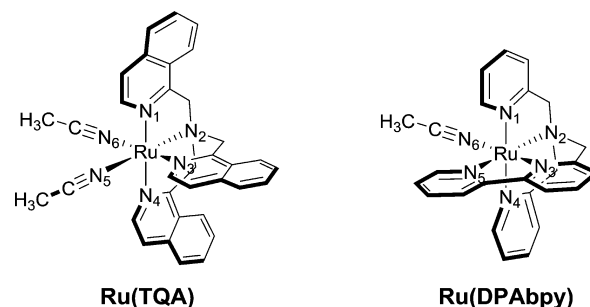
and characterized by UV−vis and ^{1}H nuclear magnetic resonance (NMR) spectroscopies and X-ray crystallography.[45] Upon irradiation with >395 nm light for 1−3 h, these complexes exhibited different ligand dissociation behaviors as determined by changes in the UV−vis and ^{1}H NMR spectra. Ru(TQA) has two MeCN ligands at N5 and N6 (Scheme 1). The photodissociation of MeCN occurred only at N6, where the MeCN is perpendicular to the plane of the quinolines (Q) at N1 and N4. The other MeCN at N5, which is coplanar to Q at N1 and N4, did not dissociate. Ru(DPAbpy) contains one MeCN at N6 that is coplanar with the bpy ligand. This complex is inert toward photodissociation of MeCN under the conditions described here.

TD-DFT calculations of the UV−vis spectrum show that the lowest-energy excited singlet states for both Ru(TQA) and Ru(DPAbpy) are ^{1}MLCT states. The ^{1}MLCT states readily convert to ^{3}MLCT states by intersystem crossing.[66] Because the photodissociations occur from the triplet states, we focused on the triplet potential energy surfaces. Because the states of interest are the lowest-energy electronic configurations in the triplet manifold, they can be calculated by SCF methods as well as by TD-DFT methods.

The SCF-optimized geometries of the ground state (S$_0$) and triplet excited states in acetonitrile are listed in Table 1. The optimized geometries in water agree closely with the acetonitrile values (see Table S1 of the Supporting Information). The structures, relative energies, spin densities, and molecular orbitals for the triplet states of Ru(TQA) are shown in Figures 1−3; the corresponding data for Ru-(DPAbpy) are shown in Figures 4−6. The ^{3}MLCT states

Table 1. Calculated Bond Lengths (angstroms) and Angles (degrees) of Ru Complexes in the S_0, ^{3}MLCT, ^{3}MC, and ^{3}TS^a States in Acetonitrile

	Ru–N1	Ru–N2	Ru–N3	Ru–N4	Ru–N5	Ru–N6	N1–Ru–N4	N2–Ru–N5	N3–Ru–N6
Ru(TQA)									
S_0 (calcd)	2.085	2.077	2.062	2.085	2.010	2.023	162.8	178.0	177.1
S_0 (X-ray[45])	2.067	2.052	2.042	2.061	2.042	2.032	163.8	178.9	174.0
^{3}MLCT	2.038	2.068	2.050	2.089	2.035	2.049	164.2	178.0	173.2
^{3}MC$_1$^{b}	2.118	2.088	2.146	2.141	2.014	–	116.2	179.8	–
^{3}MC$_2$	2.424	2.350	2.066	2.161	2.084	2.015	142.2	151.9	175.7
^{3}MC$_3$^{b}	2.103	2.349	2.078	2.101	–	2.106	151.3	–	176.1
^{3}TS	2.082	2.092	2.123	2.164	2.017	2.454	150.1	178.6	164.0
Ru(DPAbpy)									
S_0 (calcd)	2.089	2.111	1.979	2.088	2.075	2.030	162.7	162.6	177.8
S_0 (X-ray[45])	2.061	2.084	1.953	1.986	2.052	2.053	164.6	163.4	177.1
^{3}MLCT	2.104	2.147	1.983	2.089	2.035	2.055	159.2	163.2	179.4
^{3}MC$_1$	2.380	2.360	2.020	2.161	2.113	2.024	144.9	150.7	175.1
^{3}MC$_2$^{b}	2.091	2.135	2.165	2.098	2.099	–	163.4	152.9	–

^{a}^{3}TS is the optimized transition structure for the conversion of ^{3}MLCT to ^{3}MC$_1$. ^{b}Five-coordinate ^{3}MC structure that has released one acetonitrile.
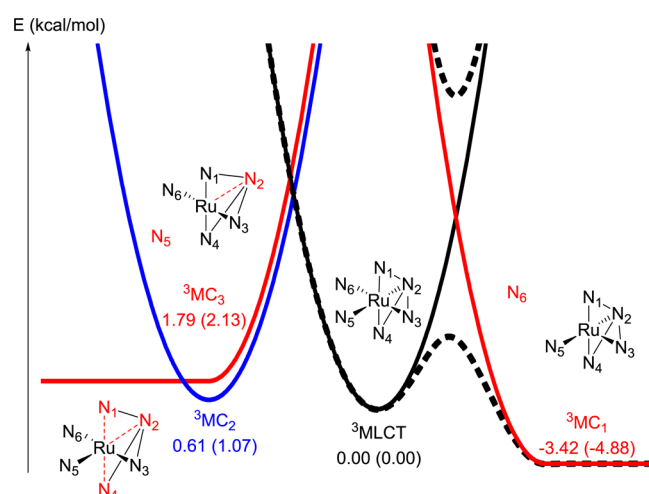

Figure 1. Relative energies in kilocalories per mole of the ^{3}MLCT and ^{3}MC structures on the triplet potential energy surface for Ru(TQA) in acetonitrile. The data in parentheses are the relative energies in water. The energy of the ^{3}MLCT state is arbitrarily set to zero (while the relative energies and barriers are drawn to scale, the shapes of the potential energy curves are only schematic).
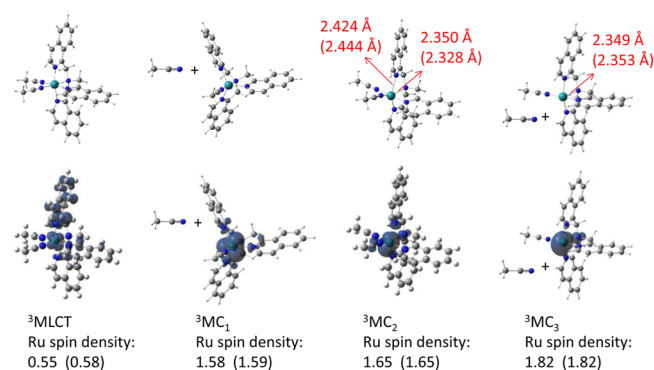

Figure 2. Optimized structures and spin density plots of the triplet states for the Ru(TQA) complex in acetonitrile. The data in parentheses are for calculations in water.

have geometries similar to those of ground states, and the changes in the Ru−N bond lengths are small, ranging from
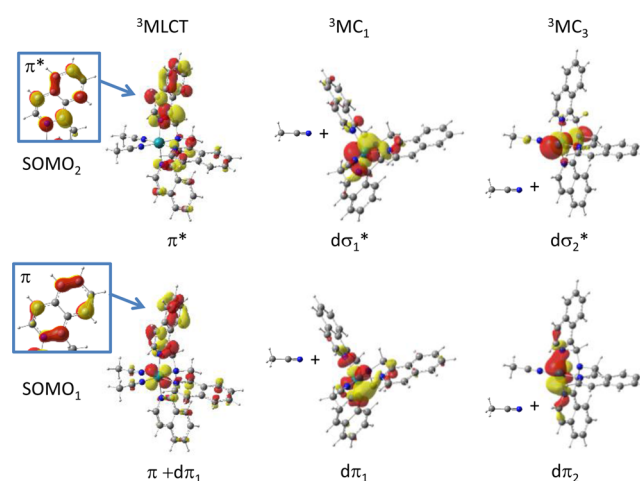

Figure 3. Isosurface plots of SOMO$_1$ and SOMO$_2$ in the optimized structures of the excited Ru(TQA) complexes in acetonitrile. Insets provide SOMO$_1$ and SOMO$_2$ plots of quinoline at N1 in ^{3}MLCT (the singly occupied corresponding/biorthogonal orbitals can be found in Figure S1 of the Supporting Information).

0.001 to 0.06 Å. The ^{3}MLCT states have one unpaired electron on Ru and one on the ligand. The spin density on Ru in the ^{3}MLCT state for Ru(DPAbpy) is 0.82, while the spin density of 0.55 on Ru for Ru(TQA) is significantly lower because of mixing between the metal-based SOMO$_1$ (dπ_1) of the ^{3}MLCT state and the π orbital of TQA. At the optimized geometries of the ^{3}MLCT states, vertical excitation calculations by TD-DFT and ΔSCF show that all of the ^{3}MC electronic configurations are higher in energy than the ^{3}MLCT state for both Ru(TQA) and Ru(DPAbpy).

The ^{3}MC structures have dσ* orbitals occupied, so these electronic configurations can be found by starting from the ^{3}MLCT geometries and stretching some of the Ru−N bonds. Different ^{3}MC structures show the elongation of different Ru−N bonds and the bending of different N−Ru−N bond angles compared to those of the ^{3}MLCT state. The optimized geometries of the lowest ^{3}MC structures of Ru(TQA) and Ru(DPAbpy) are listed in Table 1 and shown in Figures 2 and 5. At the optimized geometries, one of the ^{3}MC structures for Ru(TQA) is lower in energy than the ^{3}MLCT state at its
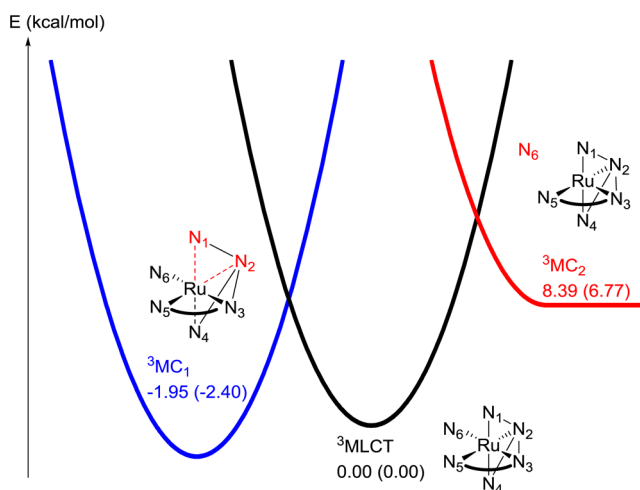
Figure 4. Relative energies of the ^{3}MLCT and ^{3}MC structures on the triplet potential energy surface for Ru(DPAbpy) in acetonitrile. The data in parentheses are the relative energies in water. The energy of the ^{3}MLCT state is arbitrarily set to be zero (while the relative energies and barriers are drawn to scale, the shapes of the potential energy curves are only schematic).
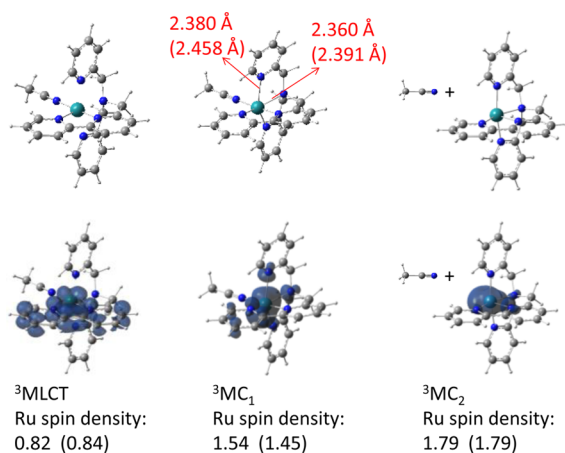

Figure 5. Optimized structures and spin density plots for the triplet states of the Ru(DPAbpy) complex in acetonitrile. The data in parentheses are for calculations in water.
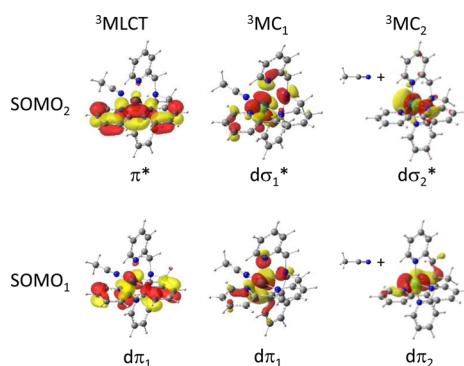

Figure 6. Isosurface plots of SOMO$_1$ and SOMO$_2$ for the optimized structures of excited Ru(DPAbpy) complexes in acetonitrile (the singly occupied corresponding/biorthogonal orbitals can be found in Figure S2 of the Supporting Information).

optimized geometry (Figure 1). The Mulliken spin densities on Ru for the three lowest ^{3}MC structures of Ru(TQA) are 1.58,

1.65, and 1.82, respectively (Figure 2). The Ru(DPAbpy) complex has two ^{3}MC structures, and Ru spin densities are 1.54 for ^{3}MC$_1$ and 1.79 for ^{3}MC$_2$ (Figure 5).

Relative Energies of the ^{3}MLCT and ^{3}MC structures. The photodissociation of ligands from these complexes has been attributed to internal conversion from the ^{3}MLCT state to a dissociative ^{3}MC state.[49] If the dissociative ^{3}MC state is the lowest-lying state on the triplet surface, the photochemical process is more likely to result in ligand dissociation. Figure 1 shows the relative energies of the optimized ^{3}MLCT and ^{3}MC geometries of the Ru(TQA) complex. The relative energies are somewhat sensitive to the functional used in the calculations. For the BP86 functional, the lowest ^{3}MC structure is 3–5 kcal/mol below the ^{3}MLCT state. During the optimization of the six-coordinate ^{3}MC$_1$ complex, the Ru−N6(MeCN) bond elongates, leading to dissociated products of acetonitrile and a five-coordinate [Ru(TQA)MeCN]$^{2+}$ complex. In addition, the two quinolines at N1 and N4 are markedly bent toward N6. As shown in Table 1, the N1−Ru−N4 angle decreases from 164° in ^{3}MLCT to 116° in ^{3}MC$_1$. This ^{3}MC structure of Ru(TQA) with MeCN dissociated corresponds to a five-coordinate, trigonal bipyramidal complex and correlates with the photodissociation of MeCN from N6 observed in the NMR experiments. The optimization of the corresponding ^{3}MC electronic configuration of [Ru(TQA)(MeCN)(H$_2$O)]$^{2+}$, where water has replaced the acetonitrile at N6, also leads to release of water and formation of the same five-coordinate, trigonal bipyramidal complex.

During the optimization of the six-coordinate ^{3}MC$_3$ structure, the Ru−N5(MeCN) distance elongates and leads to dissociated products. The Ru−N2(amine) bond is significantly lengthened to 2.35 Å [compared to 2.068 Å in the ^{3}MLCT state (Table 1)]. However, the dissociated ^{3}MC$_3$ products are 1.79 kcal/mol higher in energy than the ^{3}MLCT state, whereas the ^{3}MC$_1$ dissociated products are 3.42 kcal/mol lower (Figure 1). This indicates that the formation of ^{3}MC$_3$, and hence dissociation of MeCN from N5, is thermodynamically less favorable than that of ^{3}MC$_1$ and dissociation of MeCN from N6. This is consistent with the experimental results that show that efficient photodissociation of MeCN occurs at N6 rather than N5 of the Ru(TQA) complex. In addition to the relative energies of the ^{3}MLCT and ^{3}MC structures, the rates for internal conversion to the ^{3}MC surfaces and subsequent dissociation will also depend on the reorganization energy and on possible interactions between the ^{3}MLCT and ^{3}MC electronic configurations (discussed below).

The difference between the ^{3}MLCT and ^{3}MC structures can be understood in terms of their different singly occupied molecular orbitals (SOMOs) shown in Figure 3 [the singly occupied corresponding/biorthogonal orbitals are essentially the same as the canonical SOMOs (see Figure S1)]. In the ^{3}MLCT state, the lower-energy SOMO (SOMO$_1$) is a dπ_1 orbital of Ru mixed with a π orbital of the quinoline at N1, while the higher-energy SOMO (SOMO$_2$) is mainly a π^* orbital of the quinoline ring. The ^{3}MC structures show elongation of different Ru−N bonds, and this can be understood in terms of the different patterns of SOMOs (Figure 3). In the lowest-energy ^{3}MC$_1$ structure, the Ru−N6(MeCN) bond dissociates and SOMO$_2$ has Ru dσ_1^* (d$_{x^2-y^2}$ like) character, while SOMO$_1$ is a dπ_1 orbital of Ru similar to SOMO$_1$ of the ^{3}MLCT state. In the higher-energy ^{3}MC$_3$ configuration, the Ru−N5 bond dissociates and both SOMOs

are different from the SOMOs in the ^{3}MLCT state: SOMO$_1$ is a dπ_2 orbital of Ru, while SOMO$_2$ is primarily a dσ_2* (d$_{z^2}$-like) orbital of Ru.

The energies, structures, spin densities, and SOMOs of the triplet states for Ru(DPAbpy) are shown in Figures 4−6 and Table 1. The dissociated ^{3}MC$_1$ structure is 2 kcal/mol lower in energy than the ^{3}MLCT state in acetonitrile and exhibits significant elongation of the Ru−N1(pyridyl) and Ru−N2(amine) bonds (2.380 and 2.360 Å, respectively). Figure 6 shows that SOMO$_2$ is a dσ* orbital that is antibonding with N1 and N2. The optimization of the six-coordinate ^{3}MC$_2$ structure results in elongation of the Ru−N6(MeCN) distance, leading to dissociation of MeCN. However, the dissociated products are 8 kcal/mol higher in energy than the ^{3}MLCT state in acetonitrile. The fact that this structure is higher in energy than the ^{3}MC$_1$ and ^{3}MLCT structures is in accord with the experimental results that ligand photodissociation of MeCN is not observed for this complex.

In summary, the optimized geometries and relative energies of the ^{3}MLCT and dissociative ^{3}MC states of Ru(TQA) and Ru(DPAbpy) are consistent with the results of photodissociation experiments. In Ru(TQA), the dissociative ^{3}MC state corresponding to Ru−N6(MeCN) elongation is lower than the ^{3}MLCT state, while the one corresponding to Ru−N5(MeCN) elongation is higher than the ^{3}MLCT state. In Ru(DPAbpy), the dissociative ^{3}MC state is higher than the ^{3}MLCT state. The experiments found that efficient photodissociation of MeCN occurred from the N6 position of Ru(TQA) but not from the N5 position, while MeCN photodissociation was observed seen for Ru(DPAbpy).

Potential Energy Scans on the Triplet Surface. To obtain energy barriers for photodissociation of MeCN, we conducted relaxed potential energy scans starting from the ^{3}MLCT state and stretching specific Ru−N(MeCN) bonds. For each scan, the chosen Ru−N bond was increased in increments of 0.1 Å and the energy was minimized with respect to the remaining coordinates. In the region around the maximum, the relaxed scan was conducted with smaller increments. Figure 7 shows the potential energy scans of Ru(TQA) with respect to the stretching of the two Ru−N(MeCN) bonds. When the Ru−N6(MeCN) bond is elongated (Figure 7a), a smooth transition occurs from the ^{3}MLCT to the dissociative ^{3}MC$_1$ state with a barrier of ∼4.7 kcal/mol (other functionals could result in a lower barrier, depending on the energy difference obtained for the ^{3}MLCT and ^{3}MC structures). The spin density on Ru increases gradually from 0.57 in ^{3}MLCT to 1.33 at the highest energy point of the scan and continues to increase to 1.58 in the dissociated products.

To gain a better description of the dissociation, the transition structure (^{3}TS) was optimized with the QST3 method. The initial guess for ^{3}TS was taken from the highest point of the scan. The optimized transition state is 4.6 kcal/mol higher in energy than the ^{3}MLCT minimum energy structure, and ^{3}TS possesses one imaginary frequency, corresponding to MeCN dissociating from the N6 position of Ru(TQA). The optimized ^{3}TS structure is shown in Figure 8. For an acetonitrile solution, the Ru−N6(MeCN) bond length is 2.454 Å and the N1−Ru−N4 angle of ^{3}TS (150.1°) is between the values for the ^{3}MLCT state (164.2°) and the dissociated ^{3}MC structure (116.2°) (see Table 1). The optimized ^{3}TS has a spin density of 1.33 on Ru (Figure 8), which is closer to the dissociated ^{3}MC$_1$ state (1.58)
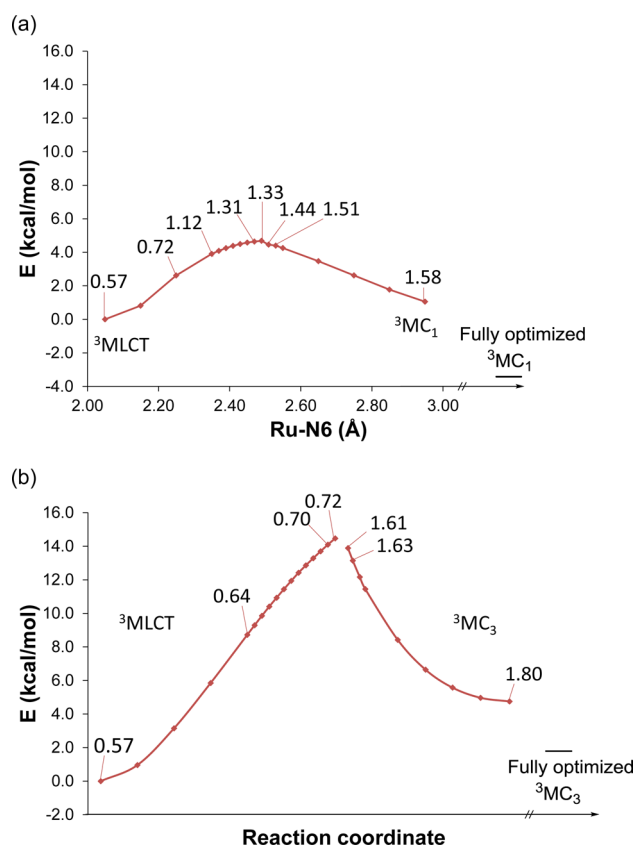

Figure 7. Relaxed potential energy scans from the ^{3}MLCT state of Ru(TQA) in acetonitrile for (a) stretching the Ru−N6(MeCN) coordinate and (b) stretching the Ru−N5(MeCN) coordinate on the ^{3}MLCT surface, an abrupt transition to the ^{3}MC state, and a steepest descent reaction path toward the ^{3}MC$_3$ potential energy surface. The energy of each point is relative to the energy of the fully optimized ^{3}MLCT geometry. The numbers along the scan show the spin density on Ru.
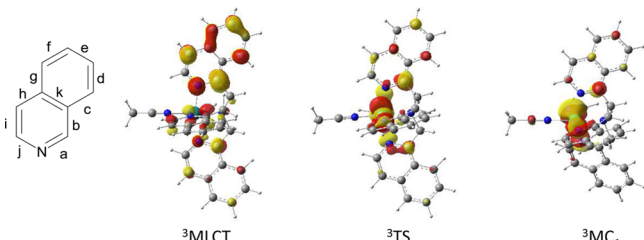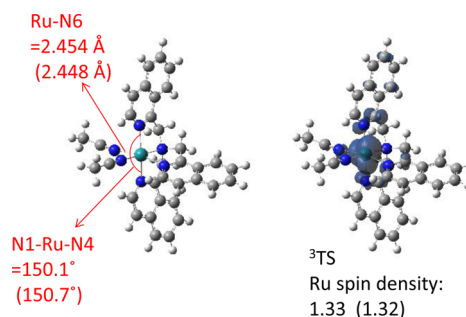

Figure 8. Optimized geometry and spin density plot for ^{3}TS in acetonitrile. The data in parentheses are for calculations in water.

than to the ^{3}MLCT state (0.55). The bond lengths in the N1 quinoline ring for ^{3}MLCT, ^{3}TS, and ^{3}MC$_1$ are shown in Table 2. The a, d, f, and h bond lengths in the ^{3}MLCT structure are 1.415, 1.403, 1.411, and 1.440 Å, respectively, while they are shorter in the ^{3}MC$_1$ structure because of π antibonding character of SOMO$_2$ for these bonds in ^{3}MLCT (Table 2). In contrast, SOMO$_2$ is π bonding for the e and g bonds, so they are shorter in ^{3}MLCT than in ^{3}MC$_1$. In the optimized ^{3}TS, most of the electron population has transferred to Ru, so the lengths of these bonds are closer to those of the ^{3}MC$_1$ structure.

Table 2. Bond Lengths of the Quinoline at N1 and Isosurface Plots of SOMO$_2$ (isovalue = 0.04) in the ^{3}MLCT, ^{3}TS, and Dissociated ^{3}MC$_1$ States of the Ru(TQA) Complex in Acetonitrile

^{3}MLCT ^{3}TS ^{3}MC$_1$

	a	b	c	d	e	f	g	h	i	j	k
S$_0$	1.355	1.430	1.430	1.388	1.423	1.387	1.425	1.423	1.379	1.375	1.445
^{3}MLCT	1.415	1.425	1.430	1.403	1.406	1.411	1.409	1.440	1.382	1.365	1.448
^{3}TS	1.367	1.427	1.431	1.389	1.421	1.391	1.421	1.429	1.376	1.380	1.447
^{3}MC$_1$	1.355	1.427	1.430	1.388	1.423	1.388	1.423	1.425	1.378	1.379	1.446

Elongation of the Ru−N5(MeCN) bond (Figure 7b) results in an abrupt transition from ^{3}MLCT to a higher-energy dissociative ^{3}MC$_3$ state. When the bond is stretched beyond 2.69 Å, there is a sudden switch in the occupancy of the frontier orbitals, resulting in an increase in the spin density from 0.72 to 1.61. Beyond the transition, Figure 7b shows the steepest descent reaction path on the ^{3}MC$_3$ surface. The Ru−N2 bond [*trans* to the Ru−N5(MeCN) bond] elongates by 0.35 Å, and the energy decreases by 12 kcal/mol, as the molecule relaxes toward the dissociated products (Figure 7b). These SCF calculations are confirmed by TD-DFT calculations of vertical excitation energies for points along the reaction coordinate. The TD-DFT calculations show that the ^{3}MC$_3$ potential energy curve is higher than the ^{3}MLCT potential energy curve for points along the scan prior to the transition, and ^{3}MLCT energies are higher than the ^{3}MC$_3$ energies after the transition. The barrier for the conversion of ^{3}MLCT to ^{3}MC$_3$ is estimated to be 14.5 kcal/mol, which is significantly higher than the 4.6 kcal/mol barrier found for stretching the Ru−N6(MeCN) bond and the transition to ^{3}MC$_1$. This is in agreement with the experimental results, which shows that efficient photodissociation of MeCN occurred only for N6 and not for N5.

For Ru(DPAbpy), the conversion of ^{3}MLCT to the dissociative ^{3}MC$_2$ surface is similar to that from the ^{3}MLCT to ^{3}MC$_3$ transition for Ru(TQA), showing an abrupt transition in the energy, geometry, and spin density when the Ru−N6(MeCN) bond is stretched (Figure 9). The estimated barrier is 13.1 kcal/mol, considerably higher than for the stretching of the Ru−N6(MeCN) bond in Ru(TQA) (4.6 kcal/mol). In part, this is because the dissociative products are higher in energy than the ^{3}MLCT state and in part because the rigidity of the ligand prevents relaxation of the geometry. Furthermore, there is little or no interaction between the bpy π* orbital of the ^{3}MLCT state and the Ru−N6(MeCN) σ* orbital that could lower the energy of the transition from the ^{3}MLCT state to the ^{3}MC$_2$ surface. This high barrier for Ru(DPAbpy) is in accord with experiment, which did not find photodissociation of MeCN in Ru(DPAbpy).

MO Analysis along the Potential Energy Scan. To help understand the mechanism for photodissociation for these complexes, we analyzed the MOs for relaxed geometries along the potential energy scans. For Ru(TQA), when the Ru−N6 bond is stretched longer than 2.25 Å (Figure 10), the ligand-based SOMO$_2$ mixes with the Ru $d\sigma_1$* ($d_{x^2−y^2}$-like) orbital, which corresponds to SOMO$_2$ of ^{3}MC$_1$. This orbital mixing
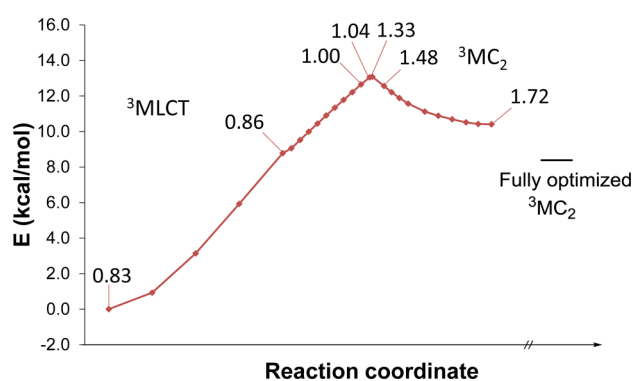

Figure 9. Relaxed potential energy scan from the ^{3}MLCT state of Ru(DPAbpy) in acetonitrile for stretching the Ru−N6(MeCN) coordinate toward dissociated products. The energy of each point is relative to the energy of the fully optimized ^{3}MLCT geometry. The numbers along the scan show the spin density on Ru.
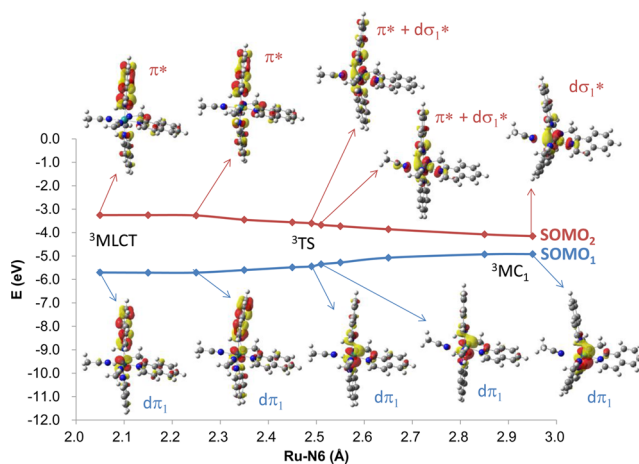

Figure 10. MO diagram for the relaxed PE scan of the triplet state of Ru(TQA) in acetonitrile along the Ru−N6(MeCN) coordinate. Selected isosurface plots of SOMOs are present to show the changes in electron population and geometry.

occurs because the π* orbital of quinoline and the $d\sigma_1$* orbital of Ru can overlap when the geometry is distorted away from octahedral coordination as the Ru−N6(MeCN) bond is stretched. This mixing promotes dissociation because the $d\sigma_1$* orbital interacts with the MeCN in an antibonding

fashion. By contrast, stretching the Ru−N5(MeCN) bond of Ru(TQA) leads to no mixing between the π^* orbital of quinoline and the $d\sigma_2^*$ (d_{z^2}-like) orbital that corresponds to SOMO$_2$ of ^{3}MC$_3$ (Figure 11). The ligand framework restricts
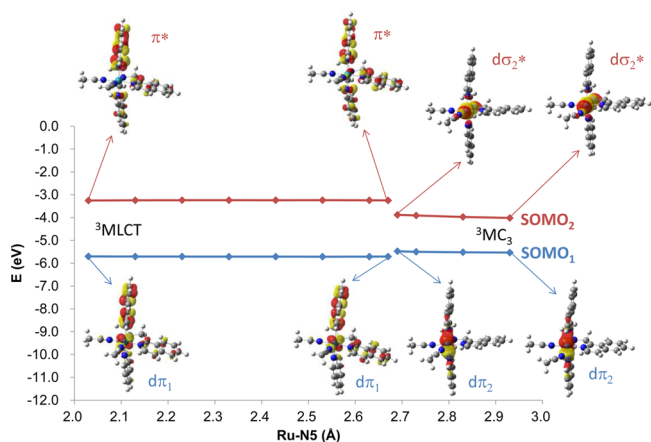

Figure 11. MO diagram for the relaxed PE scan of the triplet state of Ru(TQA) in acetonitrile along the Ru−N5(MeCN) coordinate. Selected isosurface plots of SOMOs are present to show the changes in electron population and geometry.

reorientation of the quinoline during stretching of the Ru−N5 bond, and the ligand π^* orbital remains orthogonal to the $d\sigma_2^*$ orbital. As the Ru−N5(MeCN) bond is stretched, the energy of the $d\sigma_2^*$ orbital decreases. When the energy of the $d\sigma_2^*$ orbital is lower than SOMO$_2$ of the ^{3}MLCT state, the occupancy of the two orbitals switches, resulting in an abrupt transition to the ^{3}MC$_3$ potential energy surface. Because the $d\sigma_2^*$ orbital interacts with the MeCN in an antibonding manner, this change in occupation leads to dissociation. Because there is no interaction with the π^* orbital, the Ru−N5 bond must be stretched further before the transition occurs (2.69 Å compared to 2.49 Å for Ru−N6 bond stretching). The greater amount of stretch and the lack of orbital interaction result in a higher barrier. Because breaking the Ru−N5 bond has a much higher barrier than the Ru−N6 bond, only dissociation of MeCN at N6 is observed for Ru(TQA).

A similar picture of orbital interactions is obtained when the Ru−N6(MeCN) bond of Ru(DPAbpy) is stretched (Figure 12). Because the orbitals remain orthogonal as the Ru−N6 bond is stretched, no mixing occurs between the π^* orbital of bpy and the Ru $d\sigma_2^*$ orbital responsible for MeCN dissociation. The Ru−N6 bond of Ru(DPAbpy) must be stretched by about the same amount as the Ru−N5 bond in Ru(TQA) before the $d\sigma_2^*$ orbital becomes lower in energy than SOMO$_2$ of the ^{3}MLCT state, so that the transition to the ^{3}MC$_2$ potential energy surface can occur. The similar amount of stretch results in comparable barrier heights. This high barrier is in agreement with the experiments for which photodissociation of MeCN is not detected for Ru(DPAbpy).

With the discussion given above, the selective photodissociation of acetonitrile can be rationalized as outlined in Scheme 2. Ligand photodissociation is ascribed to the conversion of ^{3}MLCT to ^{3}MC, which involves transfer of electron density from the ligand π^* orbital to a Ru $d\sigma^*$ orbital. The ease of this conversion is related to the extent of interaction (mixing) between these two orbitals. If they can interact as the bond is stretched and the complex is distorted,
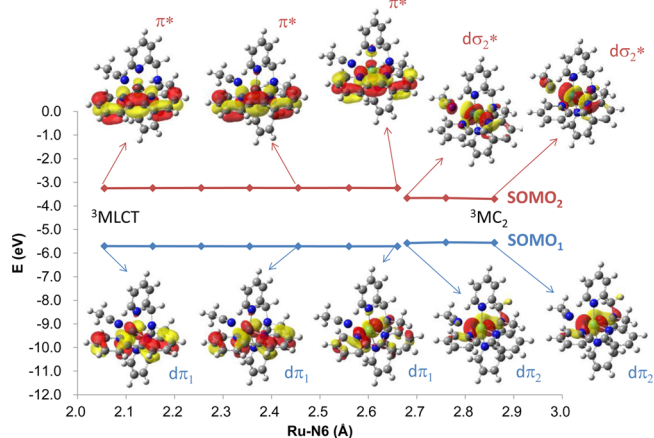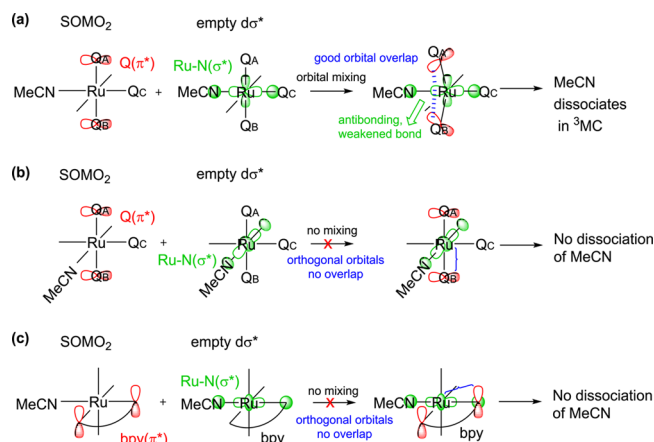

Figure 12. MO diagram for the relaxed PE scan of the triplet state of Ru(DPAbpy) in acetonitrile along the Ru−N6(MeCN) coordinate. Selected isosurface plots of SOMOs are present to show the changes in electron population and geometry.

Scheme 2. Symmetries and Orbital Interactions of SOMO$_2$ in the ^{3}MLCT States and the Empty $d\sigma^*$ Orbital[a]

[a](a) MeCN perpendicular to quinoline rings in Ru(TQA). (b) MeCN coplanar to quinoline rings in Ru(TQA). (c) MeCN coplanar to bpy in Ru(DPAbpy).

the mixing leads to a smaller barrier for ligand dissociation. If the orbitals remain orthogonal as the bond is stretched, there is no mixing and the states change abruptly when the energy of the $d\sigma^*$ orbital becomes lower than that of the ligand π^* orbital. Because reaching this geometry requires greater stretching of the bond, the barriers are higher than when mixing can occur. In Ru(TQA), there are two MeCN ligands that could dissociate. Because the MeCN at N6 in Ru(TQA) is perpendicular to quinoline rings (Q$_A$ and Q$_B$ in Scheme 2), mixing of the ligand π^* and Ru $d\sigma^*$ can occur as the bond is stretched, resulting in a smooth transition from ^{3}MLCT to ^{3}MC$_1$ and a lower barrier for photodissociation. On the other hand, for the dissociation of a MeCN coplanar with a π acceptor ligand [N1−N2−N4−N5 plane in Ru(TQA) or N2−N3−N5−N6 plane in Ru(DPAbpy)], no mixing is possible between the ligand π^* and Ru $d\sigma^*$ orbitals, causing higher barriers and a sudden transition between the ^{3}MLCT and ^{3}MC potential energy surfaces. As a result, efficient photodissociation of MeCN from N5 in Ru(TQA) or N6 in Ru(DPAbpy) is not observed.

CONCLUSIONS

Experiments have shown that suitably designed ruthenium complexes can release nitrile ligands by photoactivation. We have chosen two complexes to study the factors that govern the photodissociation in these complexes. For Ru(TQA), one of the two possible MeCN ligands is observed to dissociate selectively, whereas photodissociation of MeCN is not seen for the closely related Ru(DPAbpy) complex. We have used density functional theory to compute the energies and geometries of the ^{3}MLCT and dissociative ^{3}MC states and to explore the triplet potential energy surfaces. By analyzing the molecular orbitals along relaxed scans for stretching the Ru—N(MeCN) bonds, we have demonstrated that MeCN photo-dissociation is facilitated by orbital mixing between the ligand π^* orbital of the ^{3}MLCT state and the dσ^* orbitals that characterize the dissociative ^{3}MC states. The degree of mixing depends on the spatial relation of MeCN and π^* orbitals of the ligand. Mixing is significant when the Ru—N(MeCN) bond perpendicular to a π acceptor ligand is stretched and the complex is distorted to allow good orbital overlap. For Ru(TQA), this results in a smooth and continuous transition from the ^{3}MLCT to the ^{3}MC potential energy surface with a small barrier for photodissociation of MeCN from N6. By contrast, when the Ru—N(MeCN) bond coplanar with the π acceptor ligand is stretched [N5 in Ru(TQA) and N6 in Ru(DPAbpy)], the ligand π^* and Ru dσ^* orbitals remain orthogonal; no mixing occurs, and the barrier for the transition from ^{3}MLCT to the corresponding ^{3}MC potential energy surface is high. As a result, MeCNs coplanar with the π acceptor ligand do not dissociate upon light activation. The existence of a small barrier for conversion of ^{3}MLCT to the lowest ^{3}MC$_1$ surface for $[\text{Ru(TQA)(MeCN)}_2]^{2+}$ (4.6 kcal/mol = 30 $k_B T$ at 77 K) is consistent with the long emission decay lifetime (125 μs) and the large emission quantum yield (0.45) observed at 77 K. The examples in this study show how the electronic properties of metal complexes influence the photodissociation processes and may provide guidance for the design of new transition metal complexes for the light-activated release of ligands.

ASSOCIATED CONTENT

Ⓢ Supporting Information

The Supporting Information is available free of charge on the ACS Publications website at DOI: 10.1021/acs.inorg-chem.5b01202.

> Calculated bond lengths and angles of Ru complexes in the S$_0$, ^{3}MLCT, ^{3}MC, and ^{3}TS structures optimized in water, singly occupied corresponding/biorthogonal orbitals for ^{3}MLCT and ^{3}MC structures, and Cartesian coordinates for the S$_0$, ^{3}MLCT, ^{3}MC, and ^{3}TS structures (PDF)

AUTHOR INFORMATION

Corresponding Author

*E-mail: hbs@chem.wayne.edu.

Notes

The authors declare no competing financial interest.

ACKNOWLEDGMENTS

REFERENCES

(1) Malouf, G.; Ford, P. C. *J. Am. Chem. Soc.* **1974**, *96*, 601.
(2) Ciesienski, K. L.; Franz, K. J. *Angew. Chem., Int. Ed.* **2011**, *50*, 814.
(3) Ford, P. C.; Wink, D.; Dibenedetto, J. *Prog. Inorg. Chem.* **1983**, *30*, 213.
(4) Schatzschneider, U. *Eur. J. Inorg. Chem.* **2010**, *2010*, 1451.
(5) Garner, R. N.; Gallucci, J. C.; Dunbar, K. R.; Turro, C. *Inorg. Chem.* **2011**, *50*, 9213.
(6) Sgambellone, M. A.; David, A.; Garner, R. N.; Dunbar, K. R.; Turro, C. *J. Am. Chem. Soc.* **2013**, *135*, 11274.
(7) Schatzschneider, U. *Inorg. Chim. Acta* **2011**, *374*, 19.
(8) Ciesienski, K. L.; Hyman, L. M.; Yang, D. T.; Haas, K. L.; Dickens, M. G.; Holbrook, R. J.; Franz, K. J. *Eur. J. Inorg. Chem.* **2010**, *2010*, 2224.
(9) Ossipov, D.; Gohil, S.; Chattopadhyaya, J. *J. Am. Chem. Soc.* **2002**, *124*, 13416.
(10) Haas, K. L.; Franz, K. J. *Chem. Rev.* **2009**, *109*, 4921.
(11) Smith, N. A.; Sadler, P. J. *Philos. Trans. R. Soc., A* **2013**, *371*, ZZZ.
(12) Boerner, L. J. K.; Zaleski, J. M. *Curr. Opin. Chem. Biol.* **2005**, *9*, 135.
(13) Farrer, N. J.; Salassa, L.; Sadler, P. J. *Dalton Trans.* **2009**, 10690.
(14) Singh, T. N.; Turro, C. *Inorg. Chem.* **2004**, *43*, 7260.
(15) Barragán, F.; López-Senín, P.; Salassa, L.; Betanzos-Lara, S.; Habtemariam, A.; Moreno, V.; Sadler, P. J.; Marchán, V. *J. Am. Chem. Soc.* **2011**, *133*, 14098.
(16) Howerton, B. S.; Heidary, D. K.; Glazer, E. C. *J. Am. Chem. Soc.* **2012**, *134*, 8324.
(17) Wachter, E.; Heidary, D. K.; Howerton, B. S.; Parkin, S.; Glazer, E. C. *Chem. Commun.* **2012**, *48*, 9649.
(18) Liu, Y.; Hammitt, R.; Lutterman, D. A.; Joyce, L. E.; Thummel, R. P.; Turro, C. *Inorg. Chem.* **2009**, *48*, 375.
(19) Holder, A. A.; Zigler, D. F.; Tarrago-Trani, M. T.; Storrie, B.; Brewer, K. J. *Inorg. Chem.* **2007**, *46*, 4760.
(20) Dhar, S.; Nethaji, M.; Chakravarty, A. R. *Inorg. Chem.* **2005**, *44*, 8876.
(21) Swavey, S.; Brewer, K. J. *Inorg. Chem.* **2002**, *41*, 6196.
(22) Sears, R. B.; Joyce, L. E.; Ojaimi, M.; Gallucci, J. C.; Thummel, R. P.; Turro, C. *J. Inorg. Biochem.* **2013**, *121*, 77.
(23) Ford, P. C.; Bourassa, J.; Lee, B.; Lorkovic, I.; Miranda, K.; Laverman, L. *Coord. Chem. Rev.* **1998**, *171*, 185.
(24) Rose, M. J.; Mascharak, P. K. *Inorg. Chem.* **2009**, *48*, 6904.
(25) Halpenny, G. M.; Mascharak, P. K. *Inorg. Chem.* **2009**, *48*, 1490.
(26) Rose, M. J.; Mascharak, P. K. *Coord. Chem. Rev.* **2008**, *252*, 2093.
(27) Madhani, M.; Patra, A. K.; Miller, T. W.; Eroy-Reveles, A. A.; Hobbs, A. J.; Fukuto, J. M.; Mascharak, P. K. *J. Med. Chem.* **2006**, *49*, 7325.
(28) Patra, A. K.; Mascharak, P. K. *Inorg. Chem.* **2003**, *42*, 7363.
(29) Mitchell-Koch, J. T.; Reed, T. M.; Borovik, A. S. *Angew. Chem., Int. Ed.* **2004**, *43*, 2806.
(30) Works, C. F.; Jocher, C. J.; Bart, G. D.; Bu, X.; Ford, P. C. *Inorg. Chem.* **2002**, *41*, 3728.
(31) Salierno, M.; Marceca, E.; Peterka, D. S.; Yuste, R.; Etchenique, R. *J. Inorg. Biochem.* **2010**, *104*, 418.
(32) Filevich, O.; Salierno, M.; Etchenique, R. *J. Inorg. Biochem.* **2010**, *104*, 1248.
(33) del Marmol, J.; Filevich, O.; Etchenique, R. *Anal. Chem.* **2010**, *82*, 6259.
(34) De Candia, A. G.; Marcolongo, J. P.; Etchenique, R.; Slep, L. D. *Inorg. Chem.* **2010**, *49*, 6925.
(35) Fino, E.; Araya, R.; Peterka, D. S.; Salierno, M.; Etchenique, R.; Yuste, R. *Front. Neural Circuits* **2009**, *3*, 1.
(36) Salierno, M.; Fameli, C.; Etchenique, R. *Eur. J. Inorg. Chem.* **2008**, *2008*, 1125.

(37) Zayat, L.; Noval, M. G.; Campi, J.; Calero, C. I.; Calvo, D. J.; Etchenique, R. *ChemBioChem* **2007**, *8*, 2035.

(38) Zayat, L.; Salierno, M.; Etchenique, R. *Inorg. Chem.* **2006**, *45*, 1728.

(39) Zayat, L.; Baraldo, L.; Etchenique, R. *Imaging in Neuroscience and Development* **2005**, 391.

(40) Nikolenko, V.; Yuste, R.; Zayat, L.; Baraldo, L. M.; Etchenique, R. *Chem. Commun.* **2005**, 1752.

(41) Zayat, L.; Calero, C.; Albores, P.; Baraldo, L.; Etchenique, R. *J. Am. Chem. Soc.* **2003**, *125*, 882.

(42) Respondek, T.; Sharma, R.; Herroon, M. K.; Garner, R. N.; Knoll, J. D.; Cueny, E.; Turro, C.; Podgorski, I.; Kodanko, J. J. *ChemMedChem* **2014**, *9*, 1306.

(43) Respondek, T.; Garner, R. N.; Herroon, M. K.; Podgorski, I.; Turro, C.; Kodanko, J. J. *J. Am. Chem. Soc.* **2011**, *133*, 17164.

(44) Sharma, R.; Knoll, J. D.; Martin, P. D.; Podgorski, I.; Turro, C.; Kodanko, J. J. *Inorg. Chem.* **2014**, *53*, 3272.

(45) Sharma, R.; Knoll, J. D.; Ancona, N.; Martin, P. D.; Turro, C.; Kodanko, J. J. *Inorg. Chem.* **2015**, *54*, 1901.

(46) Liu, Y.; Turner, D. B.; Singh, T. N.; Angeles-Boza, A. M.; Chouai, A.; Dunbar, K. R.; Turro, C. *J. Am. Chem. Soc.* **2009**, *131*, 26.

(47) Salassa, L.; Garino, C.; Salassa, G.; Gobetto, R.; Nervi, C. *J. Am. Chem. Soc.* **2008**, *130*, 9590.

(48) Salassa, L.; Garino, C.; Salassa, G.; Nervi, C.; Gobetto, R.; Lamberti, C.; Gianolio, D.; Bizzarri, R.; Sadler, P. J. *Inorg. Chem.* **2009**, *48*, 1469.

(49) Sun, Q.; Mosquera-Vazquez, S.; Sufffren, Y.; Hankache, J.; Amstutz, N.; Daku, L. M. L.; Vauthey, E.; Hauser, A. *Coord. Chem. Rev.* **2015**, *282-283*, 87−99.

(50) Becke, A. D. *Phys. Rev. A: At., Mol., Opt. Phys.* **1988**, *38*, 3098.

(51) Perdew, J. P. *Phys. Rev. B: Condens. Matter Mater. Phys.* **1986**, *33*, 8822.

(52) Frisch, M. J.; Trucks, G. W.; Schlegel, H. B.; et al. *Gaussian Development Version*, revision H.35; Gaussian, Inc.: Wallingford, CT, 2014. Complete citation in the Supporting Information.

(53) Andrae, D.; Häußermann, U.; Dolg, M.; Stoll, H.; Preuß, H. *Theoret. Chim. Acta* **1990**, *77*, 123.

(54) Dunning, T. H., Jr.; Hay, P. J. In *Modern Theoretical Chemistry*; Schaefer, H. F., III, Ed.; Plenum: New York, 1976; Vol. 3, p 1.

(55) Igel-Mann, G.; Stoll, H.; Preuss, H. *Mol. Phys.* **1988**, *65*, 1321.

(56) Francl, M. M. *J. Chem. Phys.* **1982**, *77*, 3654.

(57) Hariharan, P. C.; Pople, J. A. *Theoret. Chim. Acta* **1973**, *28*, 213.

(58) Marenich, A. V.; Cramer, C. J.; Truhlar, D. G. *J. Phys. Chem. B* **2009**, *113*, 6378.

(59) Dennington, R.; Keith, T.; Millam, J. M. *GaussView*, version 5; Semichem, Inc.: Shawnee Mission, KS, 2009.

(60) Neese, F. *J. Phys. Chem. Solids* **2004**, *65*, 781.

(61) Peng, C.; Ayala, P. Y.; Schlegel, H. B.; Frisch, M. J. *J. Comput. Chem.* **1996**, *17*, 49.

(62) Peng, C.; Bernhard Schlegel, H. B. *Isr. J. Chem.* **1993**, *33*, 449.

(63) Hratchian, H. P.; Schlegel, H. B. *J. Phys. Chem. A* **2002**, *106*, 165.

(64) Casida, M. E.; Jamorski, C.; Casida, K. C.; Salahub, D. R. *J. Chem. Phys.* **1998**, *108*, 4439.

(65) Stratmann, R. E.; Scuseria, G. E.; Frisch, M. J. *J. Chem. Phys.* **1998**, *109*, 8218.

(66) McCusker, J. K. *Acc. Chem. Res.* **2003**, *36*, 876.